Insights into microstructural evolution from nanocrystalline SnO_2 thin films prepared by pulsed laser deposition

Z. W. Chen,* J. K. L. Lai, and C. H. Shek
Department of Physics and Materials Science, City University of Hong Kong, Tat Chee Avenue, Kowloon Tong, Hong Kong, People's Republic of China

(Received 19 September 2003; revised manuscript received 14 May 2004; published 21 October 2004)

Low-dimensional nanostructures of SnO_2 thin films with the interesting features of the tetragonal rutile structure have been prepared by pulsed laser deposition. The microstructural evolution of nanocrystalline SnO_2 thin films has been investigated using x-ray diffraction, transmission electron microscopy, high-resolution transmission electron microscopy, and Raman spectroscopy. Experimental results indicate that the as-prepared SnO_2 thin films appear to be of polycrystalline state, have a large amount of defects, such as oxygen vacancies, vacancy clusters, and local lattice disorder at the interface and surface, and the appearance of a new Raman peak. It suggests that this new Raman peak is closely related to a surface layer of nonstoichiometic SnO_x with different symmetries than SnO_2, or in other words, the new peak marks an additional characteristic of space symmetry of the grain agglomeration of nanocrystalline SnO_2. The study of the microstructural evolution of nanocrystalline SnO_2 is significant for the understanding of the whole structure feature of nanomaterials and for the fabrication of new nanomaterials with favorable properties.

DOI: 10.1103/PhysRevB.70.165314 PACS number(s): 81.15.Fg, 61.72.Dd, 81.07.Bc, 68.37.Lp

I. INTRODUCTION

Low-dimensional systems, such as nanocrystallites, thin films, two-dimensional heterostructures, clusters, and surface layers, demonstrate a variety of physical, chemical, and functional properties different from those of bulk materials.[1,2] The influence of grain size on material properties is especially remarkable for polycrystalline thin films.[3] Tin dioxide, SnO_2, is an *n*-type semiconductor with a wide band gap (E_g=3.6 eV, at 300 K) and well known for its applications in gas sensors,[4,5] dye-based solar cells,[6] transparent conducting electrodes,[7] and catalyst supports.[8] In recent years, the nanocrystalline SnO_2 has been reported to have some different characteristics from the bulk crystals, and much attention has been focused on the synthesis of SnO_2 nanowires,[9] nanotubes,[9] nanorods,[10,11] and nanobelts[12–14] and exploration of their novel properties. A variety of methods, such as sol-gel,[15,16] chemical vapor deposition,[17,18] magnetron sputtering,[19] sonochemical,[20] and thermal evaporation,[21] have been employed to prepare SnO_2 thin films or nanoparticles. The use of polycrystalline SnO_2 as transparent electrodes and solid-state gas sensor is attracting much interest with regard to the relationships between its electrical properties and crystallite size.[1,2]

In the past few years, the interface and surface microstructure of nanomaterials have been extensively and intensively investigated. Diversified types of interface-structure models have also been proposed for nanostructural materials,[8,22,23] such as the gaslike model and order and extended order models. It is common that the peculiar properties of nanomaterials are explained in terms of the interface and surface structures, while the effects from the microstructure of the grains are neglected. In fact, for different preparation methods, the microstructure of nanomaterials can be nanocrystallite, nanoamorphous grain, or nanocluster agglomerations with some crystalline features. Since the grains are the basic components of nanomaterials, changes in their microstructure should inevitably change the physical and chemical properties. Therefore, study of the microstructure of grains can help us reveal the general structure of nanomaterials and explain the corresponding experimental results. It is expected that the microstrucural evolution may represent important building blocks for nanodevices and may offer exciting opportunities for both fundamental research and technological applications.

The Raman techniques can reveal local structural information on amorphous and poorly crystallized samples. Usually, the disorder induces spectral changes, which are discussed in reference to the bulk crystal spectra and on their vibrational density of states. Tin oxide gives rise to well-defined Raman spectra,[24] and the dynamics of rutilelike compounds has been extensively studied.[24–26] However, for nanocrystallites, the surface atoms represent a non-negligible fraction of atoms and give rise to specific spectral changes. The corresponding frequencies of the optical modes have been theoretically calculated and experimentally measured.[27] When the SnO_2 grain size is small, the Raman spectrum is modified, at least partially. Several authors have reported that the existence of some Raman peaks, which have been found to be closely related to grain size.[28–32] However, some of these reports cannot adequately explain the origin of the abnormal spectrum.

The purpose of this paper is to characterize the crystalline structural changes and the microstructure evolution of nanocrystalline SnO_2 thin films by x-ray diffraction (XRD), x-ray photoelectron spectra (XPS), transmission electron microscopy (TEM), high-resolution transmission electron microscopy (HRTEM), and Raman spectroscopy. We found that there is an increase in *a* and a decrease in *c* for the as-prepared SnO_2 thin films prepared by pulsed laser deposition. Interestingly, a new Raman peak was observed for the first. It suggests that this new Raman peak is closely related to a surface layer of nonstoichiometic SnO_x with different symmetries than SnO_2, or in other words, the new peak

marks an additional characteristic of space symmetry of the grain agglomeration of nanocrystalline SnO_2.

II. EXPERIMENTS

The target for pulsed laser deposition (PLD) was a sintered SnO_2 disk. The method employed to synthesize the pure SnO_2 powder is described by the direct oxidation reaction at 1050 °C—viz., $Sn+O_2 \rightarrow SnO_2$—carried out in a horizontal quartz tube. SnO_2 thin films were prepared by pulsed laser deposition techniques. The circular target was consisted of high-purity cassiterite SnO_2 (99.8%). The size of the target was about $\phi 15\ \text{mm} \times 4\ \text{mm}$, and it was cleaned with methanol in an ultrasonic cleaner before installation to minimize contamination. The laser used was a KrF excimer laser (Lambda Physik, LEXtra 200, Germany) producing pulse energies of about 350 mJ at a wavelength of 248 nm and a frequency of 10 Hz. The duration of every excimer laser pulse was 34 ns. The laser energy was transmitted onto the target in a high-vacuum chamber through an ultraviolet (UV-) grade fused silica window using an UV-grade fused silica lens. During the experiment, the target was rotating at a rate of 15 rpm to avoid drilling. The fluence was set at 5 J/cm^2 per pulse, corresponding to a total of approximately 1.5×10^5 laser pulses. The growth rate was estimated to be about 3×10^{-1} nm/s (or about 1 μm/h) and the as-prepared thin-film thickness was about 4 μm. The ablated substance was collected on a glass substrate, which was mounted on a substrate holder 2.5 cm away from the target. The high vacuum in the deposition chamber was achieved by using a cryopump (Edwards Coolstar 800). The base pressure prior to laser ablation was about 1×10^{-6} mbar, and the working pressure during laser ablation was about 2×10^{-6} mbar. All deposition processes were carried out at ambient temperature.

Raman scattering measurements were obtained by backscattering geometry with a SPEX-1403 laser Raman spectrometer. The excitation source was an argon-ion laser operated at a wavelength of 514.5 nm in the backscattering configuration and a low incident power to avoid thermal effects. XRD was performed with a Philips X'pert diffractometer using Cu $K\alpha$ radiation (1.5406 Å) in reflection geometry. Proportional counter with an operating voltage of 40 kV and a current of 40 mA was used. XRD patterns were recorded at a scanning rate of 0.05 deg s^{-1} in the 2θ ranges from 15° to 65°. A Philips CM20 transmission electron microscope operating at an acceleration voltage of 200 kV was used to determine the grain size distribution of the thin films. HRTEM images of nanocrystalline SnO_2 were obtained with a JEOL-2010 high-resolution transmission electron microscope with a point-to-point resolution 1.94 Å operating at 200 kV, and with energy-dispersive x-ray spectroscopy (EDS). The lattice images and the agglomerate states of the nanocrystalline SnO_2 were further carefully analyzed. The x-ray photoelectron measurements were performed in a VG ESCALAB MK-II electron spectrometer with a base pressure of 1×10^{-7} Pa. Clean sample surfaces were obtained by scraping them *in situ* with a diamond file in ultrahigh vacuum. X-ray photoelectron spectra were taken by using a monochromatized x-ray source of Mg $K\alpha$ radiation ($h\nu = 1253.6$ eV). The energy resolution was about 0.9 eV. All the measurements were carried out at room temperature.

III. RESULTS AND DISCUSSION

Tin dioxide has a tetragonal rutile crystalline structure (known in its mineral form as cassiterite) with point group D_{4h}^{14} and space group $P4_2/mnm$. The unit cell consists of two metal atoms and four oxygen atoms. Each metal atom is situated amidst six oxygen atoms which approximately form the corners of a regular octahedron. Oxygen atoms are surrounded by three tin atoms which approximate the corners of an equilateral triangle. The lattice parameters are $a = 4.7382(4)$ Å and $c = 3.1871(1)$ Å.[27]

Figures 1(a), 1(b), and 1(c) show x-ray diffraction patterns of the commercial SnO_2 bulks, as-prepared, and annealed at 300 °C for 30 min SnO_2 thin films, respectively. The SnO_2 average grain sizes were calculated using the TEM micrograph and the Scherrer formula $D = K\lambda/\beta \cos\theta$, respectively, where D is the diameter of the nanoparticles, $K = 0.9$, λ (Cu $K\alpha$) = 1.5406 Å, and β is the full width half maximum of the diffraction lines. Both results show that the average grain sizes of the as-prepared and the annealing SnO_2 nanoparticles are about 8 and 12 nm, respectively. Figure 2 shows a TEM bright-field image and the corresponding selected-area electron diffraction (SAED) pattern (inset) of the as-prepared SnO_2 thin film. The particle sizes observed in the micrographs are larger than those estimated from XRD data, indicating significant agglomeration of the particles. As seen in the TEM bright-field image, there are many small particles of roughly spherical shape. The contrast of the particles in different regions of the TEM image indicates different density, which may be related to the grain sizes. The polycrystalline diffraction rings of the SAED pattern (inset in Fig. 2) also demonstrate the microstructural characteristics of the typical tetragonal SnO_2 thin films ($d_{200} = 2.37$ Å, $d_{210} = 2.12$ Å, $d_{310} = 1.50$ Å, and $d_{202} = 1.32$ Å). The crystallites close to Bragg orientations were recognizable by their dark contrast. The interplanar spacings agree well with those of the tetragonal rutile structure shown in Table I, and it confirms the XRD data. For the as-prepared SnO_2 thin film [see Fig. 1(b)], it can be seen that the peaks were broadened. This indicates that the SnO_2 average grain size was smaller than that of the bulk materials. For the annealing SnO_2 thin film [see Fig. 1(c)], it can be seen that the peaks became sharp. This indicates that the SnO_2 average grain size increased with heat treatment. It is known that, for the tetragonal structure, the lattice parameters can be calculated by

$$d_{hkl} = \frac{1}{\sqrt{\frac{h^2+k^2}{a^2} + \frac{l^2}{c^2}}}, \tag{1}$$

where h, k, and l are all integers, (hkl) is the lattice plane index, and a and c are lattice constants. For a real crystal, the calculated values of a and c are the same based on different crystal planes. However, the presence of a large number of vacant lattice sites and local lattice disorders may lead to

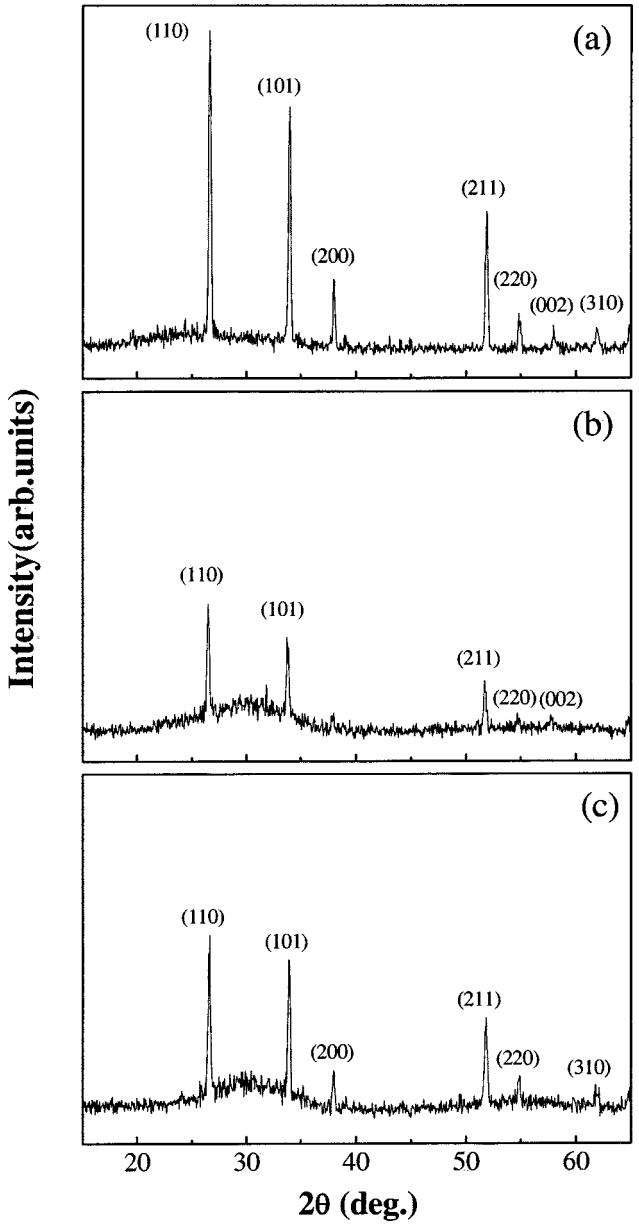

FIG. 1. X-ray diffraction patterns of SnO_2 thin films. (a) The commercial SnO_2 bulks, (b) the as-prepared SnO_2 thin film, and (c) annealing SnO_2 thin film.

obvious reduction in intensities (or even the disappearance) of the XRD peaks of the some lattice planes [e.g., the lattice planes (200), (220), (002), (310), etc., in Fig. 1(b)]. Therefore, these results imply destroyed periodicities in some crystal planes and a significant distortion of the rutile lattice. We have calculated the lattice parameters with different samples using Eq. (1). The results have been shown in Table II. From Table II, we can easily notice the relationship of the grain sizes with the changes of lattice parameters. Comparing Ref. 27, the commercial SnO_2 bulks, and the as-prepared nanocrystalline SnO_2 thin film, we found that there is an increase in a and a decrease in c for the as-prepared SnO_2 thin films prepared by the PLD method. This implies that the as-prepared thin films may exhibit a large number of oxygen vacancies, vacancy clusters, and local lattice disorder, which

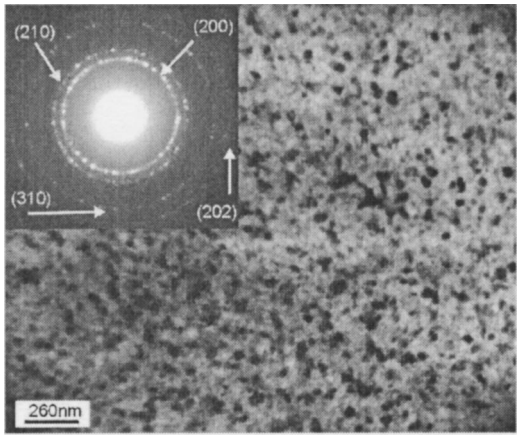

FIG. 2. TEM bright-field image of the as-prepared nanocrystalline SnO_2 thin film shows the fine grains of SnO_2 thin films; selected-area electron diffraction (SAED) pattern (inset) corresponding to the tetragonal rutile structure shows the microstructural characteristics of the polycrystalline SnO_2 thin film.

lead to an increase in a and a decreases in c.

Figures 3(a), 3(b), and 3(c) show the room-temperature Raman spectra of the commercial SnO_2 bulk materials, as-prepared, and annealed at 300 °C for 30-min nanocrystalline SnO_2 thin films, respectively. In general, SnO_2 with the rutile structure belongs to the space group D_{4h}^{14}, of which the normal lattice vibration at the Γ point of the Brillouin zone is given as follows on the basis of group theory:[32]

$$\Gamma = \Gamma_1^+(1A_{1g}) + \Gamma_2^+(1A_{2g}) + \Gamma_3^+(1B_{1g}) + \Gamma_4^+(1B_{2g}) + \Gamma_5^-(1E_g) + \Gamma_1^-(1A_{2u}) + 2\Gamma_4^-(B_{1u}) + 3\Gamma_5^+(E_u). \quad (2)$$

In order to investigate the characteristics of Raman spectra, Fig. 4 depicts the symmetries of the optic modes of the rutile structure for zero wave vector. Among these vibrations, the symmetry A_{2g} and B_{1u} modes are optically inactive, while symmetry A_{2u} and E_u modes are infrared active. The remain-

TABLE I. Relationship of the interplanar spacing (d_{hkl}) of index (hkl) in the direct lattice for different samples.

Samples	Ref. 27 d_{hkl} (Å)	As-prepared thin films d_{hkl} (Å)	Commercial bulks d_{hkl} (Å)
110	3.347	3.3608	3.3422
101	2.6427	2.6536	2.6347
200	2.369	2.3720	2.3660
111	2.3094		
210	2.1189		
211	1.7641	1.7667	1.7603
220	1.6750	1.6823	1.6738
002	1.5934	1.5964	1.5901
310	1.4984		1.4932
221	1.4829		
112	1.4392		
301	1.4155		

TABLE II. Relationship of the lattice parameters for different samples.[a]

Samples	Ref. 27	As-pepared thin films	Commercial bulks
a_{110} (Å)	4.733	4.753	4.727
a_{200} (Å)	4.738	4.744	4.732
Δa (Å)	−0.005	0.009	−0.005
$c_{101\text{-}110}$ (Å)	3.186	3.198	3.173
$c_{101\text{-}200}$ (Å)	3.184	3.201	3.172
Δc (Å)	0.002	−0.003	0.001

[a]a_{110} and a_{200} are calculated with XRD peaks (110) and (200), respectively; $c_{101\text{-}110}$ and $c_{101\text{-}200}$ are calculated with XRD peaks (101), (110), and (200), respectively; Δa and Δc are the difference of a_{110}, a_{200} and $c_{101\text{-}200}$, respectively.

ing optic modes A_{1g}, B_{1g}, B_{2g}, and E_g are Raman active in first order with the polarizability tensors:[33]

$$\alpha(A_{1g}) = \begin{pmatrix} a & 0 & 0 \\ 0 & a & 0 \\ 0 & 0 & b \end{pmatrix}, \quad \alpha(B_{1g}) = \begin{pmatrix} c & 0 & 0 \\ 0 & -c & 0 \\ 0 & 0 & 0 \end{pmatrix},$$

$$\alpha(B_{2g}) = \begin{pmatrix} 0 & f & 0 \\ f & 0 & 0 \\ 0 & 0 & 0 \end{pmatrix}, \quad \alpha(E_g) = \begin{pmatrix} 0 & 0 & d \\ 0 & 0 & d \\ d & d & 0 \end{pmatrix}. \qquad (3)$$

It can be seen from Fig. 3(b) that the Raman intensity is strongest for the mode A_{1g} at 636.3 cm^{-1}, followed by the mode B_{2g} at 780.9 cm^{-1} and the mode E_g at 474.1 cm^{-1}; the data of A_{1g}, B_{2g}, and E_g modes are in agreement with those observed in a previous report.[31] Thus the Raman spectra show the typical features of the rutile phase for the as-prepared SnO_2 thin film. However, the variation of the mode B_{1g} cannot be measured in the present experiments. It is that the mode B_{1g} appears quite often with smaller nanoparticles, but is difficult to locate due to its very low intensity with respect to the other modes [e.g., $0.001I$ (A_{1g})] (Ref. 33) and the existence of the low-frequency bands. The remarkable aspect of the Raman spectrum for the as-prepared SnO_2 thin film [see Fig. 3(b)] is the appearance of a new Raman peak at about 516.1 cm^{-1}. This new Raman peak has not been observed in the previous reports. In order to explore whether or not this new Raman peak comes from the nanocrystalline SnO_2, the as-prepared SnO_2 thin film has been annealed at 300 °C for 30 min. Figure 3(c) shows the Raman spectrum of the nanocrystalline SnO_2 thin film annealed at 300 °C for 30 min. The remarkable aspect of the Raman spectrum is that this new Raman peak disappears in annealing SnO_2 thin film. This result agrees well with the theoretical predication that the vibrational modes have been investigated in the high-frequency region of 542–486 cm^{-1} by Diéguez *et al.*[31] Thus we attribute this phenomenon to the microstructural evolution which results to the surface disorder of nanoparticles in nanocrystalline SnO_2 thin films. In theory, this vibrational mode can be attributed to disorder activation of the Raman forbidden mode.[3] The appearance of this new peak indicates that it arises either as a consequence of reducing particle dimensions (prepared by PLD techniques) or due to the conversion from amorphous to crystalline material. However, since the SnO_2 nanoparticles are crystalline for the complete range of sizes analyzed in the present work, the appearance of this new peak cannot be related to the amorphous to crystal transition. Therefore, the contribution of this new peak may be considered a consequence of reducing particle dimensions and hence the abnormal behavior of the surface and interface of nanocrystalline SnO_2.

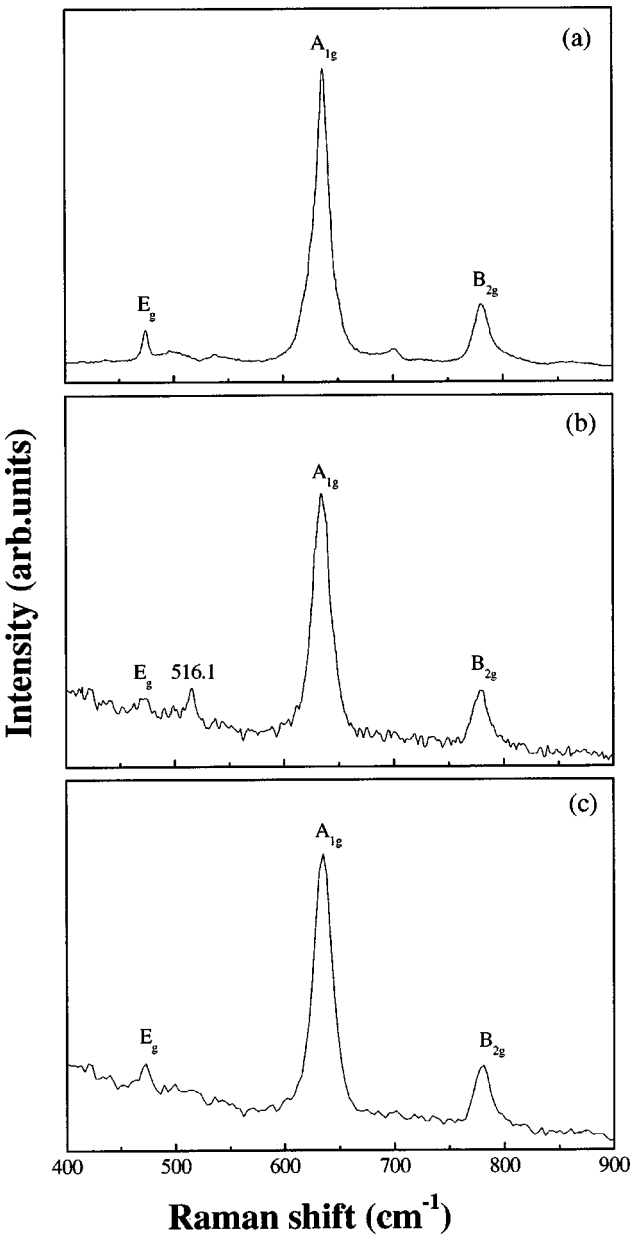

FIG. 3. Room-temperature Raman spectra of (a) SnO_2 bulk materials, (b) the as-prepared nanocrystalline SnO_2 thin film, and (c) annealing SnO_2 thin film.

In fact, the Raman active is sensitively dependent on the surface disorder—e.g., the oxygen defects and composition in the surface region. Figures 5(a) and 5(b) show the O 1*s* core-level spectra of the as-prepared nanocrystalline SnO_2 thin film and annealed at 300 °C for 30 min, respectively. Inspection reveals a dominant O 1*s* maximum at about

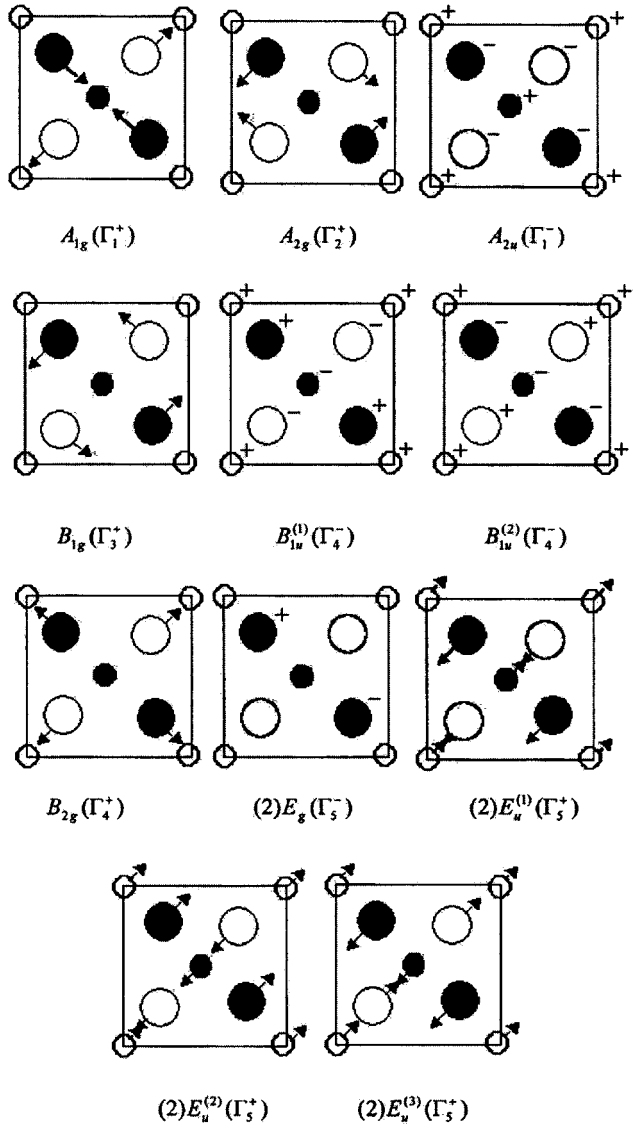

FIG. 4. Symmetries of the optic modes of the tetragonal rutile structure for zero wave vector. Labeling is in the notation of Mulliken, in parentheses, of Koster. Doubly degenerate modes are indicated by a "(2)" preceding the Mulliken symbol.

530 eV binding energy. It was found that the peak position at about 530 eV was hardly shifted with heat treatment within the range (0.9 eV) of the energy resolution. That is, the O 1*s* peak energy for the as-prepared sample was 529.9 eV shown in Fig. 5(a) and 530.1 eV for the annealing sample shown in Fig. 5(b). It was also found that the peak line shape seemed to be asymmetric and a satellite structure existed in as-prepared nanocrystalline SnO_2 thin films. It is noted that, for the as-prepared nanocrystalline SnO_2 thin films, the O 1*s* core level exhibits its major peak at 529.9 eV with a clear shoulder at about 2–3 eV higher binding energy shown in Fig. 5(a). The half-peak widths were about 2.9 and 2.0 eV for the as-prepared and annealing samples, respectively. This indicated that the peak width decreased with heat treatment and the shoulder peak disappears after heat treatment. It is suggested that the appearance of the clear shoulder peak in Fig. 5(a) was due to the surface effects of nanocrystalline

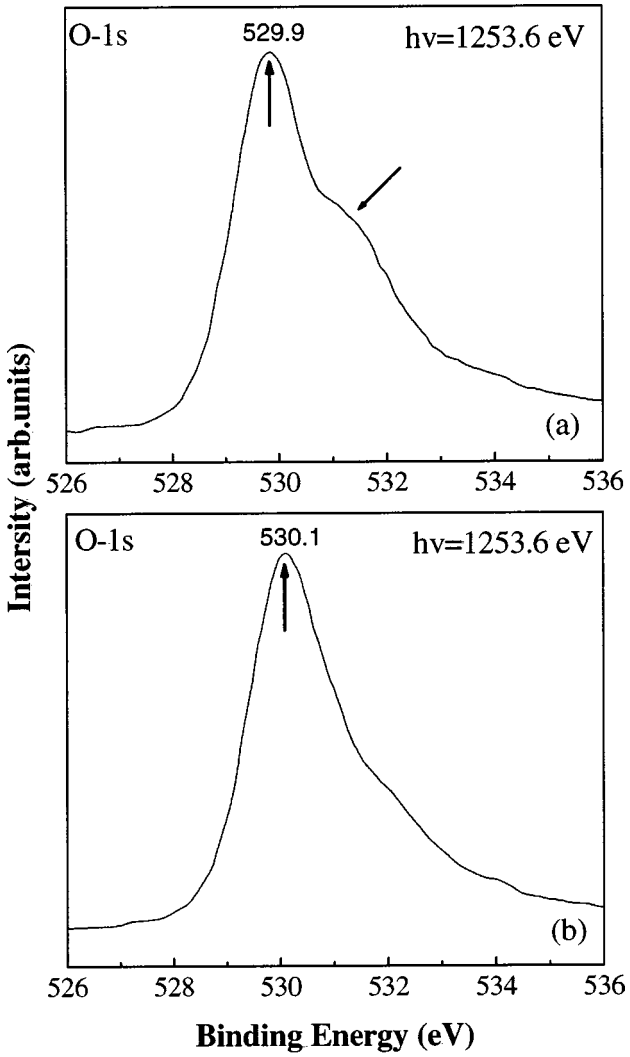

FIG. 5. O 1*s* core-level XPS spectra of nanocrystalline SnO_2 thin films. (a) As-prepared SnO_2 thin film and (b) annealing SnO_2 thin film.

SnO_2. When the grain size is small, the number of surface atoms increases greatly; for example, the surface atoms comprise 3% of the total number of atoms when the grain size is 100 nm and 30% when it is 10 nm.[34] Surface atoms are different from the inner atoms with respect to the environment of the crystal field and the binding energy and have a very large number of dangling bonds, their coordination is not completed, and they very easily combine other atoms. Therefore, a clear shoulder peak appeared in the as-prepared nanocrystalline SnO_2 thin film. The energy-dispersive x-ray spectroscopy recorded on the as-prepared nanocrystalline SnO_2 thin films is shown in Fig. 6. EDS analysis of the sample reveals that the as-prepared thin film is composed of 38.3 at. % Sn and 61.7 at. % O, which Sn:O=1:1.611 is departure to that of bulk SnO_2 (Sn:O=1:2). The Cu peaks come from the Cu grids. The above results indicate that the oxygen vacancies and nonstoichiometic SnO_x ($x<2$) relating to the as-prepared nanocrystalline SnO_2 thin films in the surface layer cause a large number of oxygen defects in the surface region.

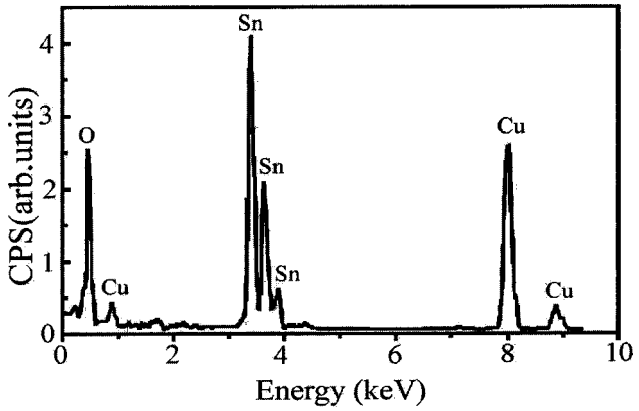

FIG. 6. EDS recorded on the as-prepared SnO_2 thin film.

In order to investigate the origin of this new Raman peak, as an indirect reasoning, Fig. 7 shows a high-resolution transmission electron micrograph of the as-prepared SnO_2 thin film prepared by the PLD method. It can be seen that the SnO_2 particles are well crystallized and the nanoparticles are characterized by a quasispherical shape. The inset at the bottom left-hand corner further exhibits a HRTEM image of a single SnO_2 nanoparticle in the as-prepared SnO_2 thin film. It presents that the SnO_2 nanoparticle is clearly crystalline with a quasispherical shape. However, we found that nanocrystalline SnO_2 grains are often overlapped and connected with two or three neighbors through necks in the as-prepared SnO_2 thin film shown in the inset at the upper right-hand corner. It indicates that there are the strong distortion of the crystalline structure and the higher degree of agglomeration in the as-prepared SnO_2 thin film. In general, when the grain size is greater than the micrometer range, its shape will depend on the dynamics of the crystal growth process, and

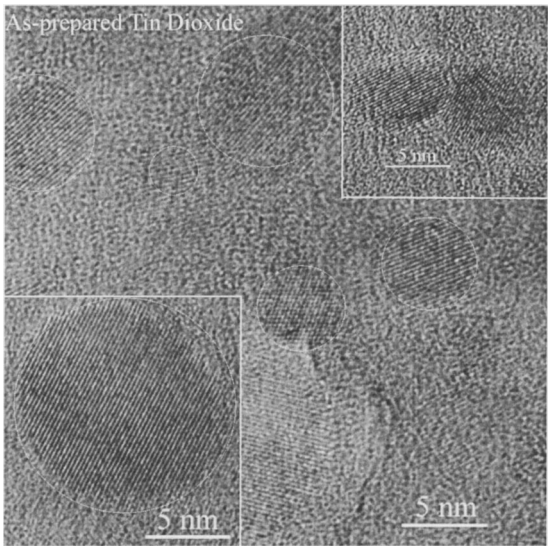

FIG. 7. HRTEM image of the as-prepared nanocrystalline SnO_2 thin films shows its crystallinity. The inset at the bottom left-hand corner further exhibits a HRTEM image of a single SnO_2 nanoparticle in the as-prepared SnO_2 thin film. The inset at the upper right-hand corner shows the agglomeration state of SnO_2 nanoparticles in the as-prepared SnO_2 thin film.

when the grain size is several nanometers, the main factor deciding its shape may be the requirement of a minimum interfacial energy. For fluids, the energy for a spherical interface is minimum; for crystals, the external crystal face is the crystal face having the lowest interfacial energy. Therefore, during the formation of nanocrystalline SnO_2, in order to maintain the minimum energy of the system, spherical nanocrystals need to be formed and the crystal face should be the one which possesses the lowest interfacial energy for the assembled grains. According to the above description, we may consider the SnO_2 nanocrystals as quasispherical. This is also supported by the HRTEM photograph of SnO_2 obtained in Ref. 8, which showed that the crystals are polygons, most of which tend to be spherical. Synchronously, in our experiment, we found that many defects, such as vacant lattice site, vacancy cluster, or local disorder at the surface and interface of nanocrystalline SnO_2, cause the lattice distortion and the lowering of lattice space symmetry.

It is known that, in a disordered crystal, it is correlated with preventing atoms from vibrating in phase and preventing their displacements by imperfections modify its space symmetry.[31] Changes in the local symmetry of the crystal produce changes in some of the components of the polarizability tensor, even for the normally forbidden vibration modes—i.e., due to the loss in long-range order all phonons are optically possible and the Raman spectrum should resemble the phonon density of states. In an intermediate case, a shift of the classical modes accompanied by broadening and the appearance of some SnO_2 forbidden modes should be observed. This is indeed what occurs with modes A_{1g}, B_{2g}, E_g, and A_{2u}. However, the band 516.1 cm^1 cannot fit any of the SnO_2 Raman-forbidden modes. The appearance of this new mode as a consequence of coupling between modes cannot explain the high contribution of this band observed in the spectrum of the smaller nanoparticles either. Furthermore, it is well known that the nanometer-sized crystalline materials have a crystalline component forming the crystallite nucleus and an interfacial component consisting of all the atoms situated at the grain boundaries between particles or at their surfaces. The latter usually has several atomic layers in which atoms are slightly displaced from the exact position that would be suggested by the crystalline structure of the material. Thus it is possible that this new Raman peak arises from this surface layer of nonstoichiometric SnO_x with different symmetries from SnO_2.[22,35] When the nanoparticle size is small, the volume occupied by the interface and surface material increases with respect to the volume occupied by core material. It has been shown that, in the extreme case of single SnO_2 crystal, surface reconstruction in the (110) surface involves up to three monolayers of atoms and the presence of oxygen vacancies.[36] This gives rise to a nonstoichiometric SnO_x at the surface and this could be responsible for producing this new peak. It is notice that this new peak is observed in SnO_2 and not in other nanocrystalline semiconductors may be due to the high reactivity of the SnO_2 surface with environmental gases.[37] To sum up, for a nanocrystalline SnO_2 grain, a large number of vacant lattice positions and local lattice disorders can lead to a change in bond length as shown Table II, a space symmetry reduction of D_{4h}^{14}, and an obvious lattice distortion. The high Raman activity of the

new vibrational mode for very small crystals, resulting from disordered SnO_x, probably, from the interaction of surface material, can be explained by the findings of Hama and Matsubara[38] and Hayashi and Yamamoto,[39] which suggest that the Raman enhancement of the shell contribution is caused by the larger vibrational amplitudes and much higher electric field in the shell than in the core. In conclusion, therefore, the disorder and nanoparticle size strongly influence the vibrational properties of this material. When the nanparticle size is small, the appearance of this new Raman peak is due to a surface layer of nonstoichiometric SnO_x with different symmetries from SnO_2.

IV. CONCLUSIONS

In summary, for the nanocrystalline SnO_2 thin film prepared by the PLD techniques, it was found that the nanocrystalline SnO_2 grain possesses some structure features of the tetragonal rutile structure, but has a large amount of defects, such as oxygen vacancies, vacancy clusters, and local lattice disorder at the interface and surface. We believe that the main reasons of the change of some x-ray diffraction peaks and the appearance of a new Raman peak are the microstructural evolution of the grain component and the lowering of lattice space symmetry. Although the investigation of the properties of this material is in progress, it is believed that the nanocrystlline SnO_2 thin films may be used to enhance the performance of gas sensor devices. By choosing suitable synthetic parameters, such as the various PLD conditions, substrate temperature, distance between the substrate and the target, oxygen partial pressure in the chamber, the heat treatment temperature and duration, heating rate, etc., may be to determine the optimum conditions for the production of this material. Our findings indicate that the *n*-type wide-band-gas semiconductor nanocrystalline thin films can be manipulated by using pulsed laser deposition techniques, offering new opportunities to control material fabrication.

ACKNOWLEDGMENT

The work described in this paper was fully supported by a grant from the Research Grant Council of the Hong Kong Special Administrative Region, China (Project No. CityU 101303).

*Electronic address: cnzwchen@yahoo.com.cn

[1] K. L. Chopra, S. Major, and D. K. Pandya, Thin Solid Films **102**, 1 (1993).
[2] D. Kohl, Sens. Actuators B **1**, 158 (1990).
[3] L. Abello, B. Bochu, A. Gaskov, S. Koudryavtseva, G. Lucazeau, and M. Roumyantseva, J. Solid State Chem. **135**, 78 (1998).
[4] G. Ansari, P. Boroojerdian, S. R. Sainkar, R. N. Karekar, R. C. Alyer, and S. K. Kulkarni, Thin Solid Films **295**, 271 (1997).
[5] S. Ferrere, A. Zaban, and B. A. Gsegg, J. Phys. Chem. B **101**, 4490 (1997).
[6] O. K. Varghese and L. K. Malhotra, Sens. Actuators B **53**, 19 (1998).
[7] Y. S. He, J. C. Campbell, R. C. Murphy, M. F. Arendt, and J. S. Swinnea, J. Mater. Res. **8**, 3131 (1993).
[8] D. Z. Wang, S. L. Wen, J. Chen, S. Y. Zhang, and F. Q. Li, Phys. Rev. B **49**, 14 282 (1994).
[9] Z. R. Dai, J. L. Gole, J. D. Stout, and Z. L. Wang, J. Phys. Chem. B **106**, 1274 (2002).
[10] Y. K. Liu, C. L. Zheng, W. Z. Wang, C. R. Yin, and G. H. Wang, Adv. Mater. (Weinheim, Ger.) **13**, 1883 (2001).
[11] C. K. Xu, G. D. Xu, Y. K. Liu, X. L. Zhao, and G. H. Wang, Scr. Mater. **46**, 789 (2002).
[12] Z. W. Pan, Z. R. Dai, and Z. L. Wang, Science **291**, 1947 (2001).
[13] Z. R. Dai, Z. W. Pan, and Z. L. Wang, Solid State Commun. **118**, 351 (2001).
[14] J. Q. Hu, X. L. Ma, N. G. Shang, Z. Y. Xie, N. B. Wong, C. S. Lee, and S. T. Lee, J. Phys. Chem. B **106**, 3823 (2002).
[15] A. Maddalena, R. D. Maschio, S. Dire, and A. Raccanelli, J. Non-Cryst. Solids **121**, 365 (1990).
[16] C. H. Shek, J. K. L. Lai, and G. M. Lin, Nanostruct. Mater. **11**, 887 (1999).
[17] R. N. Ghostagore, J. Electrochem. Soc. **125**, 110 (1978).
[18] R. D. Tarey and T. A. Raju, Thin Solid Films **128**, 181 (1995).
[19] T. Minami, H. Nanto, and S. Takata, Jpn. J. Appl. Phys., Part 2 **27**, L287 (1988).
[20] J. J. Zhu, Z. H. Lu, S. T. Aruna, D. Aurbach, and A. Gedanken, Chem. Mater. **12**, 2557 (2000).
[21] V. Schosser and G. Wind (unpublished).
[22] X. Zhu, R. Birringer, U. Herr, and H. Gleiter, Phys. Rev. B **35**, 9085 (1987).
[23] H. E. Schaefer, R. Würschum, R. Birringer, and H. Gleiter, Phys. Rev. B **38**, 9545 (1988).
[24] R. S. Katiyar, P. Dawson, M. M. Hargreave, and G. R. Wilkinson, J. Phys. C **4**, 2421 (1971).
[25] F. Gervais and W. Kress, Phys. Rev. B **31**, 4809 (1985).
[26] T. Sato and T. Asari, Jpn. J. Appl. Phys., Part 1 **64**, 1193 (1995).
[27] G. McCarthy and J. Welton, Powder Diffr. **4**, 156 (1989).
[28] J. Zuo, C. Y. Xu, X. M. Liu, C. S. Wang, C. Y. Wang, Y. Hu, and Y. T. Qian, J. Appl. Phys. **75**, 1835 (1994).
[29] C. Xie, L. Zhang, and C. Mo, Phys. Status Solidi A **141**, K59 (1994).
[30] K. N. Yu, Y. H. Xiong, Y. Liu, and C. S. Xiong, Phys. Rev. B **55**, 2666 (1997).
[31] A. Diéguez, A. Romano-Rodríguez, A. Vilà, and J. R. Morante, J. Appl. Phys. **90**, 1550 (2001).
[32] J. G. Traylor, H. G. Smith, R. M. Nicklow, and M. K. Wilkinson, Phys. Rev. B **3**, 3457 (1971).
[33] P. S. Peercy and B. Morosin, Phys. Rev. B **7**, 2779 (1973).
[34] G. H. Wang and M. Han, Prog. Phys. **10**, 248 (1990).
[35] W. Romanowski, Surf. Sci. **18**, 373 (1969).
[36] F. H. Jones, R. Dixon, J. S. Foord, R. G. Egdell, and J. B. Phetica, Surf. Sci. **376**, 367 (1997).
[37] T. Pagnier, M. Boulova, A. Galerie, A. Gaskov, and G. Lucazeau, J. Solid State Chem. **143**, 86 (1999).
[38] T. Hama and T. Matsubara, Prog. Theor. Phys. **59**, 1407 (1978).
[39] S. Hayashi and K. Yamamoto, Superlattices Microstruct. **2**, 581 (1986).